High Interharmonic Generation from Isolated Bound States

Supplementary Materials

Sergey Hazanov[1,2†], Alexey Gorlach[1†], Ron Ruimy[1], Dmitry Yakushevskiy[1], Matan Even Tzur[1], Marcelo F. Ciappina[1,3,4], and Ido Kaminer[1*]

*Ido Kaminer. Email: kaminer@technion.ac.il

Dipole moment in a 1D system

To estimate the dipole moment of two isolated bound states in a 1D potential well, we fit the parameters of an ideal two-level system (TLS) such that its non-harmonic features match those of the potential well. In essence, this implies using an external field with the same amplitude and frequency, and matching the energy separation of the TLS to that of the 1D system. Coinciding the non-harmonic features of both systems allows us to determine the dipole moment d, such that the effective Rabi frequency in the 1D system is defined as $\Omega_{\mathrm{R}}^{1\mathrm{D}} = d \cdot E$. Note that this simple approach is only possible when considering constant drive envelopes, such as in Fig. (1), where the dipole moment is found to be $d = 2.82$ in atomic units. For a resonant drive, the zero-order Mollow triplet follows a simple linear formula, and therefore in this case, the dipole moment can also be estimated by fitting two sidebands of the first harmonic.

Attosecond pulse train reconstruction

To reconstruct the attosecond pulse train associated with the emitted harmonics between $\omega_{\mathrm{start}} = h_{\mathrm{start}}\omega_{\mathrm{d}}$ and $\omega_{\mathrm{end}} = h_{\mathrm{end}}\omega_{\mathrm{d}}$, we perform the following steps:

1) Perform a Fourier transform on the dipole moment acceleration, $\ddot{d}(t)$.
2) Set fast Fourier transform of the dipole acceleration $\mathrm{FFT}\{\ddot{d}(t)\}(\omega) = 0$ for $|\omega| < \omega_{\mathrm{start}}$ and $|\omega| > \omega_{\mathrm{end}}$.
3) Perform an inverse Fourier transform.

The values of $(h_{\mathrm{start}}, h_{\mathrm{end}})$ are chosen to filter the noisy features of the low harmonics.

Two-level system localization in the extreme nonlinear regime

In this section, we discuss the TLS analog for wavepacket localization in double well potentials (also discussed in the main text). The Hamiltonian that we consider in this section is given by Eq. (8):

$$H = \frac{\omega_{\mathrm{a}}}{2}\,\sigma_z - \sigma_x \Omega_{\mathrm{R}} \cos \omega_{\mathrm{d}} t, \tag{S1}$$

The TLS is analogous to the 1D system with two isolated states. In Fig. 5 of the main text, we demonstrated that the energy degeneracy points of Eq. (2) are tightly related to the localized dynamics of the electron's wave packet. Fig. 5 depicts the mean value of $\langle \sigma_x \rangle$, averaged on the whole duration of the external field drive, $\mathrm{avg}_{t\in(0,T)}\langle \sigma_x \rangle$. Note that for an initial state $|g\rangle$ (analogous to the ground state in the 1D case), the localization changes the direction from left to right with each degeneracy point, however unlike in the 1D case, there is no transition from left-right localization around each degeneracy point (compare with the green line in Fig. 5(a)). Figure S1 depicts the correspondence between the "localization" of the TLS and the zeros of the Bessel function appearing in Eq. (2), for different initial conditions.

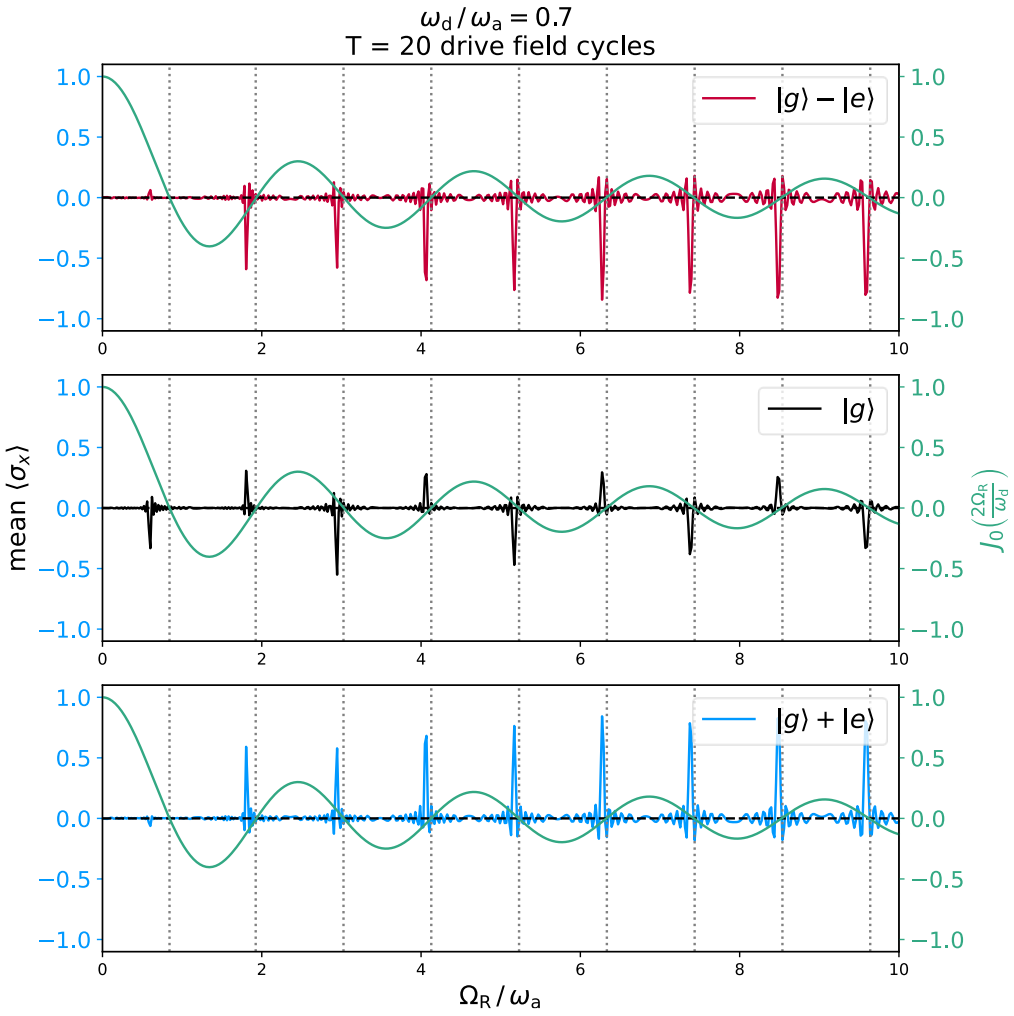

Fig. S1. Two-level system analog of localization. The different panes correspond to different initial states, $|g\rangle - |e\rangle$ (left localization), $|g\rangle$ (alternating localization), $|g\rangle + |e\rangle$ (right localization). The Schrödinger equation is solved without employing the RWA (solving Eq. (S1) directly).

Stationary potentials construction

All the potentials are constructed by summing soft Coulomb potentials, $\mathcal{V}_{\mathrm{s.c}}(x)$, given by Eq. 11 in the Methods,

$$\mathcal{V}_{\mathrm{a}}(x)=\begin{cases}\sum_{n=-\frac{N-1}{2}}^{\frac{N-1}{2}}\mathcal{V}_{\mathrm{s.c}}(x-n\cdot d,a_n,b_n) & N \text{ is odd}\\ \sum_{n=-\left(\frac{N}{2}-1\right)}^{\frac{N}{2}}\mathcal{V}_{\mathrm{s.c}}(x-n\cdot d,a_n,b_n) & N \text{ is even}\end{cases} \tag{S2}$$

where N is the number of wells, d is the distance between each adjacent well and a_n and b_n are the values of a and b (see Eq. 11 in Methods) for the nth well. In the triple-well simulation of Fig. 2c, the potential is further multiplied by $\exp(-0.05x^2)$, ensuring that the potential decays fast enough. Tab. S2 summarizes all the parameters of the stationary potentials, as well as the resonance frequency of the two lowest levels, ω_{a}, and the ionization energy, I_{p}, evaluated by solving numerically the stationary Schrödinger equation.

Evaluating the Bloch vector dynamics in 1D simulation

In Fig. 4(a2, c2) and Fig. 5(d), we present the Bloch vector dynamics of the two lowest laying bound states of an electron in a 1D potential. To compute these dynamics, we begin by numerically computing the eigenfunctions of the stationary potential, $\psi_n(x)$. Next, we compute the time-dependent wavefunction (via the Crank-Nicolson method as described in the Methods), $\psi(x,t)$. To evaluate the truncated dynamics of the lowest eigenstates of stationary potential $|\psi_0(x)\rangle$ and $|\psi_1(z)$, we compute projections

$$\begin{aligned}\alpha(t)&=\langle\psi_0(x)|\psi(x,t)\rangle,\\ \beta(t)&=\langle\psi_1(x)|\psi(x,t)\rangle.\end{aligned} \tag{S3}$$

We then define an effective TLS,

$$|\psi_{\mathrm{TLS}}(t)\rangle=\alpha(t)|0\rangle+\beta(t)|1\rangle, \tag{S4}$$

for which we can draw the Bloch vector as a function of time. Note that while $\psi_{\mathrm{TLS}}(t)$ is in general not properly normalized, i.e., $|\alpha(t)|^2+|\beta(t)|^2<1$, we perform the above procedure in simulations where occupation of other bound states, occupation of free-particle states and wavefunction absorbed in the boundaries are all negligible.

Ionization dynamics in 1D simulation

To observe the dynamics of the part of the wavefunction traversing the continuum in 1D simulations, one must consider the log magnitude of the corresponding probability density. In Fig. 4(a-d) we focused on the intra-potential dynamics for which it is more suitable to consider the probability density itself (rather than the log magnitude). Here (Fig. S2) we show the electron's wavepacket dynamics outside of binding potential (focusing on Coulomb potential simulated in Fig. 4(a-b)). In Fig. S2(a), the external field is weak enough ($E_{\max} = E_0$) so that no significant part of the wavefunction reaches the absorbing boundaries, and the wavepacket recombines (almost) fully with the ion. For a stronger external field ($E_{\max} = 1.8E_0$), large portion of the wavefunction is absorbed at the boundaries. In these simulations, the size of the spatial grid was increased to $L = 200$ a. u., however this has no significant effect on the intra-potential dynamics (which are of interest in Fig. 4(a-d)).

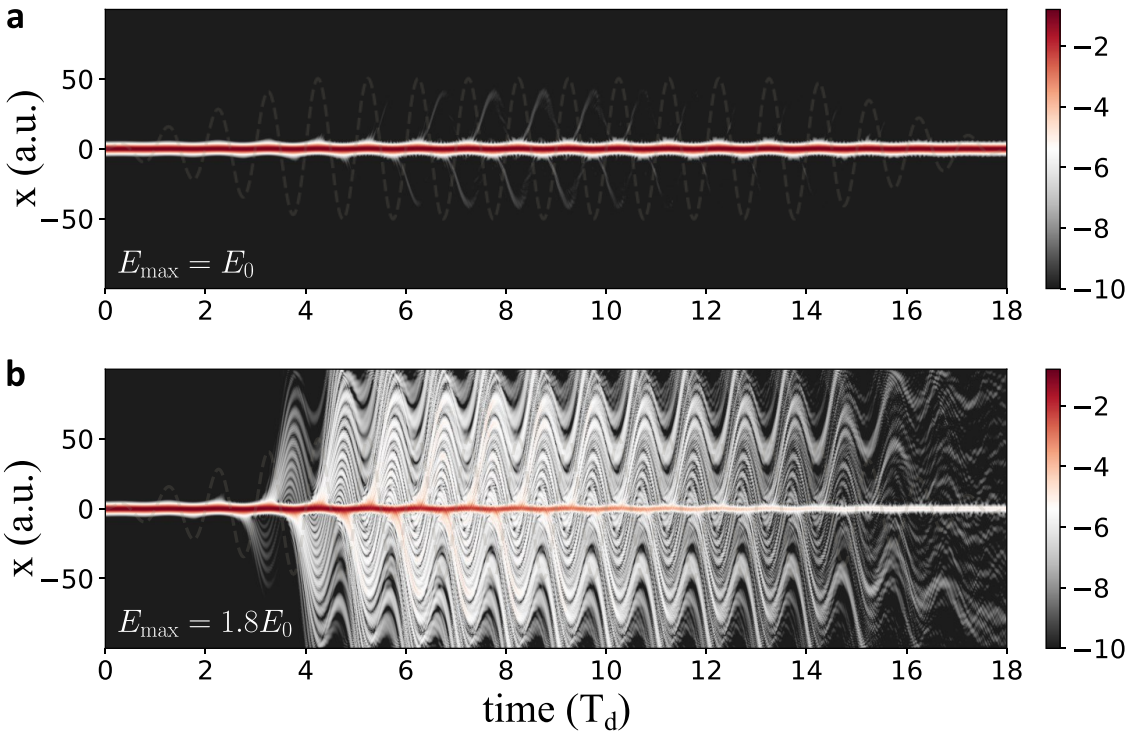

Fig. S2. Ionization dynamics in 1D simulation. The colormap indicates the log magnitude of the electron's probability density, $\log |\Psi(x,t)|^2$, as a function of x (vertical axis) and t (horizontal axis) in periods of the driving field, $T_d = 2\pi/\omega_d$. Yellow dashed lines represent the driving field with the envelope $(n_{on}, n_p, n_{off}) = (4,10,4)$ (see Methods). In (a) the maximum amplitude of the external field is $E_{\max} = E_0$ (same is in Fig. 4(a)) and in (b) the maximum field amplitude if $E_{\max} = 1.8E_0$ (same as in Fig. 4(b)).

Interharmonic generation as internal self-phase modulation mechanism

In this section we propose how to explain interharmonic generation in terms of an internal n_2 mechanism, resulting in self-phase modulation of radiation. To do so, one needs to consider temporal behavior akin to Rabi floppings. In terms of the polarization of isolated two-level systems, this modulation takes the following form (in the resonant case):

$$P \sim (\cos(\Omega_{\mathrm{R}} t) + 1)\cos(\omega_{\mathrm{d}} t),$$

which translates in the frequency domain to three spectral lines, ω_{d} and $\omega_{\mathrm{d}} \pm \Omega_{\mathrm{R}}$ (or the Mollow triplet). We conjecture that in order to capture this phenomenon, along with the carrier-wave Mollow triplets, one may consider the following form of the refractive index with internal contributions, $n(t)$ (following Eq. (8) in [6]),

$$n(t) = n_0 + n_2[E_0(\eta\cos(\Omega_{\mathrm{R}} t) + 1)\cos(\omega_d t)]^2,$$

where η quantifies the efficiency of the modulation of polarization (which in turn can probably be related to the isolation of the two-level systems, discussed in the main text).

The corresponding electric field is given by (following Eq. (4) in [6]):

$$E(t) = E_0 e^{-\frac{t^2}{\tau^2}} \cos\left(\omega_d t - \frac{\omega_d n(t) z}{c}\right).$$

The phase-modulated light could now contain the interharmonic spectral features of the carrier-wave Mollow triplets. This research avenue is interesting and calls for further exploration outside the scope of this work. In particular, the self-modulation of the light will need to take a more complicated form in the regime where the amplitude of the field surpasses the corresponding two-level system energy transition (giving rise to the helix-shaped non-harmonic lines discussed in here).

Simulations parameters

The next three tables summarize the parameters for all the simulations in the main text. The parameters are grouped according to general simulation parameters (Tab. S1), stationary potential parameters (Tab. S2), and external field parameters (Tab. S3).

Table S1. General simulation parameters for the main text.

simulation	spatial grid step	spatial grid length	temporal grid step	temporal grid length
	dx (a.u.)	L (a.u.)	dt (a.u.)	T (a.u.)
Fig. 1. c-d	0.1	50	0.1	2592
Fig. 2. a	0.1	40	0.1	5735
Fig. 2. b	0.1	40	0.1	11668
Fig. 2. c	0.1	40	0.1	7888
Fig. 3. a	0.1	40	0.2	10284
Fig. 3. c	0.1	50	0.1	2592
Fig. 4. a	0.1	50	0.1	1984
Fig. 4. b	0.1	50	0.1	1984
Fig. 4. c	0.1	50	0.1	4042
Fig. 4. d	0.1	50	0.1	5071
Fig. 5	0.1	50	0.1	2592
Fig. 6 single	0.05	50	0.021	2199
Fig. 6 double	0.05	50	0.021	2199

Table S2. Potential parameters for the main text. The values of a and b (see Eq. 11 in the methods), are specified as a tuple, each entry corresponds to the nth well (from left to right correspondingly).

simulation	number of wells	distance (a.u.)	a	b	ω_a (a.u.)	I_p (a.u.)
Fig. 1. c-d	2	6	(1, 1)	(1, 1)	0.03	0.857
Fig. 2. a	1	-	(1)	(1)	0.395	0.67
Fig. 2. b	2	5.4	(1.33, 1.33)	(1, 1)	0.04	0.767
Fig. 2. c	3	5	(1.33, 1.67, 1.33)	(1, 1, 1)	0.0319	0.659
Fig. 3. a	2	5.5	(1.25, 1.25)	(1, 1)	0.038	0.788
Fig. 3. c	2	0-6	(1, 1)	(1, 1)	0.03-0.71	0.86-1.48
Fig. 4. a-b	1	-	(1)	(1)	0.395	0.67
Fig. 4. c	2	5.4	(1.33, 1.33)	(1, 1)	0.04	0.767
Fig. 4. d	3	5	(1.33, 1.67, 1.33)	(1, 1, 1)	0.0319	0.659
Fig. 5. a-b	2	6	(1, 1)	(1, 1)	0.03	0.857
Fig. 6 single	1	-	(1)	(1)	0.395	0.67
Fig. 6 double	2	5.5	(1.72, 1.72)	(1, 1)	0.033	0.67

Table S3. External field parameters for the main text. The pulse envelope parameters, n_i, are described in the Methods.

simulation	envelope shape	$\mathbf{n_{on}}$	$\mathbf{n_p}$	$\mathbf{n_{off}}$	$\boldsymbol{\omega_d}$ $(\mathbf{a.u.})$	$\mathbf{E}$ $(\mathbf{a.u.})$
Fig. 1. c-d	trapezoidal	0.001	10	0.001	0.0242 $(0.8\omega_a)$	0-0.0534
Fig. 2. a	trapezoidal	1	50	1	0.057	0-0.0534
Fig. 2. b	trapezoidal	1	50	1	0.028 $(0.7\omega_a)$	0-0.0534
Fig. 2. c	trapezoidal	1	50	1	0.0224 $(0.7\omega_a)$	0-0.0534
Fig. 3. a	gaussian	-	20 (n_{FWHM})	-	0.027 $(0.7\omega_a)$	0-0.0534
Fig. 3. c	trapezoidal	0.001	10	0.001	0.024-0.57 $(0.8\omega_a)$	0.0534
Fig. 4. a	trapezoidal	4	10	4	0.057	0.0534
Fig. 4. b	trapezoidal	4	10	4	0.057	0.09612
Fig. 4. c	trapezoidal	4	10	4	0.028	0.0267
Fig. 4. d	trapezoidal	4	10	4	0.0224	0.0134
Fig. 5. a	trapezoidal	0.001	10	0.001	0.0242 $(0.8\omega_a)$	0-0.0534
Fig. 5. b, d	trapezoidal	0.1	10	0.1	0.0242	0.0371
Fig. 5. c	trapezoidal	0.1	10	0.1	0.0242	0.0365
Fig. 6 single	trapezoidal	2	10	2	0.04	0.04
Fig. 6 double	trapezoidal	2	10	2	0.04	0.04